Measurement of Carrier Escape Rates, Exciton Saturation Intensity, and Saturation Density in Electrically Biased Multiple-Quantum-Well Modulators

T. Sizer, II, T. K. Woodward, U. Keller, K. Sauer, T.-H. Chiu, D. L. Sivco, and A. Y. Cho

Abstract—**In this paper, we detail the results of exciton saturation intensity measurements on strained InAsP/InP and InGaAs/GaAs multiple quantum well modulators designed for 1 μm operation and under electrical bias as is required for device operation. Carrier escape times from the quantum well were also measured for both electrons and holes. These measurements allow the first experimental determination of the saturation density of the material under electrical bias. This density can also be calculated using a theoretical model proposed by Schmitt–Rink, *et al.*, [20]. The experimentally measured density is in good agreement with this theoretical model.**

I. Introduction

FREE-SPACE optical system designs offer the ability to interconnect large numbers of devices at high clock rates using simple lenses and mirrors [1]. AlGaAs/GaAs multiple-quantum-well modulators have been used in recent embodiments of these designs [2]–[4]. When using large numbers of devices at high speeds, large amounts of optical power are required. The maximum clock rate of these demonstration systems is limited by the lack of suitable high power lasers at the operating wavelength of the modulators (850nm) [2]. One solution to this problem which has had recent success is to design modulators whose operating wavelength is near neodymium based high power lasers at 1 μm [5]–[7]. Maximum clock rates in systems using these modulators will no longer be limited by available optical power, but rather by thermal [8] and saturation effects in the modulators. In this paper, we detail saturation studies performed on InGaAs/GaAs and InAsP/InP multiple-quantum-well modulators designed for 1- μm wavelength operation compatible with Nd lasers. These material systems are strained (as opposed to the AlGaAs/GaAs system which is relatively unstrained) with buffer layers used to attempt to mitigate dislocation generation and other strain effects [5]. We find that these devices have higher saturation intensities than AlGaAs/GaAs modulators measured previously. The carrier escape time from the wells plays a major role in determining the saturation intensity of the material [9]. The escape times for both carrier types were measured and used to determine the saturation density. The saturation carrier density is related to fundamental physical constants of the material. Consequently, the escape time plays a major role in determining the saturation intensity. A comparison of the saturation density with theoretical models indicates an excellent agreement. Recombination effects at strain-induced dislocations also appear to play a role in increasing the saturation intensity.

Manuscript received June 7, 1993; revised October 28, 1993.

T. Sizer, II. T. K. Woodward, U. Keller, K. Sauer, and T.-H. Chiu are with AT&T Bell Laboratories, Holmdel, NJ 07733-3030.

D. L. Sivco and A. Y. Cho are with AT&T Bell Laboratories, Murray Hill, NJ 07974-0636.

IEEE Log Number 9215752.

II. Sample Design

Five $In_xGa_{1-x}As/GaAs$ and $InAs_xP_{1-x}/InP$ multiple-quantum-well (MQW) PIN modulators were used for the work described here [5], [6]. The bandgap of these materials is tunable by varying the material parameters in the well material and can thus be matched to the wavelength of Nd-based high power lasers. The InGaAs/GaAs material system (at the $x = .26$ fraction used here) is strained with the InGaAs well material lattice constant being different from the GaAs barrier material by 1.8%. Buffer layers grown underneath the quantum well material can mitigate strain effects to some degree [5], [10]. A pair of samples with differing buffer layer designs was used to determine the effect of a buffer layer on the saturation intensity. The layer structure of these two samples is shown in Fig. 1. The quantum well structure is kept the same for the two samples (which were sequentially grown to keep all growth parameters the same) with no buffer used in sample A and a buffer layer composed of a material with a lattice constant equal to the average of the well and barrier material in sample B.[1] Since the thickness of the well and barrier are less than the critical thickness which induces dislocations and have balanced compressive and tensile strain, dislocations should only be created in the buffer layer of sample B, not in the quantum wells themselves. Previous work on these samples has indicated a strong difference in the dislocation density with heavy crosshatching on sample A indicative of a large number of dislocation lines [10].

Two other samples described in this work are really a single sample with different bias voltages applied. The layer structure for this sample (sample C, D) is shown in Fig. 1. A buffer layer

[1] Samples A and B described here are the same as samples A and B in [5]. Sample E is the same as that described in [6].

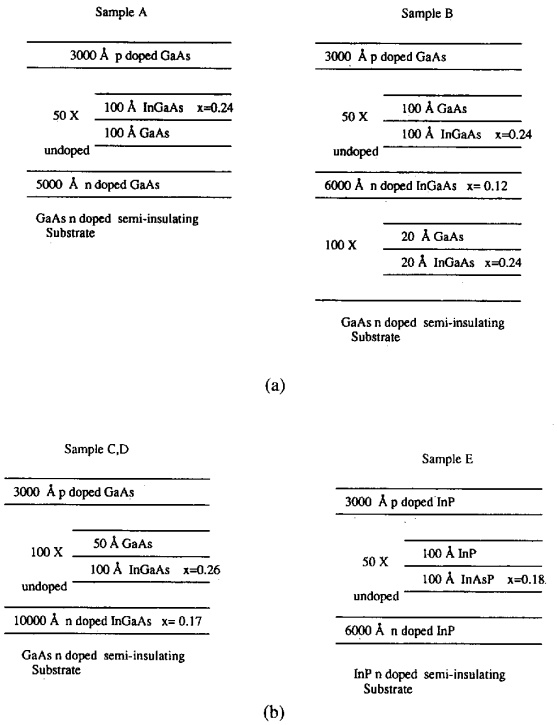

Fig. 1. Layer Designs for samples A–E.

is again used to mitigate strain effects. Mapping studies of this sample indicated fewer dislocation lines than were present in samples A or B [10].

The final sample is an InAsP/InP MQW PIN modulator [6] with a layer structure as shown for sample E in Fig. 1. The lattice mismatch between the well and barrier materials in this case os 0.6% which results in far fewer dislocations in the epitaxially grown film. Even though this design does not include a buffer layer because the level of strain is smaller, the number of dislocations is smaller than any of the other samples [10].

III. Saturation Intensity Measurements

Saturation intensities were measured using a continuous wave (CW) Nd:YLF laser operating at a wavelength of 1.054μm. All of the samples measured had zero bias exciton peaks which were at a shorter wavelength than the laser wavelength. By applying a bias voltage to the modulator the exciton peak was shifted to the laser wavelength by the quantum confined stark effect (QCSE) [11]. The absorption coefficient of the samples at the appropriate bias voltage and wavelength was determined using an auxiliary monochromator. The experimental setup used to determine the saturation intensity is shown in Fig. 2. A CW Nd:YLF laser output beam is sent to an acoustooptic modulator which selects a single 100-nanosecond pulse at a 100-kHz repetition rate. The low repetition rate and short pulses were used to minimize thermal effects [8]. A pair of polarizers and a rotating $\lambda/2$ plate provided a variable amount of intensity to reach the sample without changing the optical alignment. A calibrated pickoff and power meter were used to determine the average power on the sample while a high resolution imaging system determined the optical spot size on the sample surface. In the measurements described here, the spot size area was small (5 μm^2) and the input average power ranged up to 1 mW. Thus, the intensity on the sample surface could be accurately determined. Antireflection coatings were applied to the samples on one or both surfaces. On those samples, with only one antireflection coating, the effect of the fresnel reflection was included in determining the saturation intensity.

Experiments were performed by stepping the rotating waveplate to vary the input intensity and simultaneously measuring the input power onto, the transmission through, and the photocurrent of the modulator. Due to the effects of saturation, the transmission and photocurrent were nonlinear with respect to the input intensity in a complementary fashion. Because of the low absorption in these materials, the change in transmission due to saturation was not as great (as a percentage of transmission) as the change in photocurrent. For this reason the photocurrent data was used to determine the saturation intensity.

The saturation intensity I_{sat} is related to the model of the intensity-dependent absorption developed in [9], [12]:

$$\alpha(I_{\text{in}}) = \frac{\alpha_0}{1 + \dfrac{I_{\text{in}}}{I_s}} \tag{1}$$

where α_0 is the low-intensity-material absorption coefficient. Because there is absorption throughout the sample, however, the value for I_{in} decreases along the length of the sample. To include the decreasing input intensity effect when determining the saturation intensity from the experimental data, a formulation to fit the data was calculated. The change in intensity per unit length through the sample follows from the intensity at some point z:

$$I(z + \partial z) = I(z)e^{-\alpha(z)\partial z} \tag{2}$$

which by using (1) in the limit of small ∂z becomes

$$\frac{\partial I}{\partial z} = \frac{-I\alpha_0}{1 + \dfrac{I}{I_{\text{sat}}}} \tag{3}$$

which rearranged becomes

$$\frac{\partial I}{I} + \frac{\partial I}{I_{\text{sat}}} = -\alpha_0 \partial z. \tag{4}$$

Integrating this over the device length

$$\int_{I_{\text{in}}}^{I_{\text{out}}} \frac{1}{I} dI + \int_{I_{\text{in}}}^{I_{\text{out}}} \frac{1}{I_{\text{sat}}} dI = -\alpha_0 \int_0^L dz \tag{5}$$

which results in

$$\ln(I_{\text{out}}) - \ln(I_{\text{in}}) + \frac{I_{\text{out}} - I_{\text{in}}}{I_{\text{sat}}} = -\alpha_0 L. \tag{6}$$

If we define the transmission as $T = I_{\text{out}}/I_{\text{in}}$ and rearrange, we obtain

$$\frac{\ln(T) + \alpha_0 L}{T - 1} = \frac{-I_{\text{in}}}{I_{\text{sat}}}. \tag{7}$$

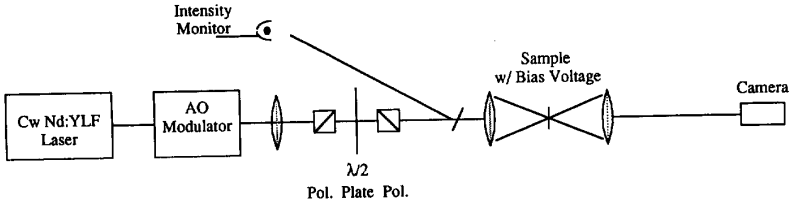

Fig. 2. Experimental setup used to make saturation measurements.

If one plots the experimental data in the manner $\ln(T) + \alpha_0 L/T - 1$ versus I_{in} then the resulting slope will be equal to $-1/I_{\text{sat}}$ and the intercept equal to zero. If one is fitting the photocurrent data instead of the transmission data one merely determines the responsivity R from the photocurrent data and uses the substitution

$$T = 1 - \frac{R}{QE} \tag{8}$$

where QE is the external quantum efficiency.[2] In this case, the linear equation becomes

$$\frac{\ln\left(1 - \dfrac{R}{QE}\right) + \alpha_0 L}{\dfrac{R}{QE}} = \frac{I_{\text{in}}}{I_{\text{sat}}} \tag{9}$$

with the slope now equal to $1/I_{\text{sat}}$. This fitting technique was used to determine the saturation intensity for all the samples. To illustrate the fitting technique the experimental data is shown in Fig. 3 and the resulting responsivity and fitting curve for sample B are shown in Fig. 4. The responsivity curve clearly shows the decreasing responsivity with increasing intensity as expected. The asymptotic value of the linear fit is not, however, equal to 0. We speculate that such loss is due to continuum bandedge or other nonexcitonic absorption which is unsaturable at these intensities. Since it is the excitonic saturation, we are trying to measure this unsaturable component is determined from the asymptote and subtracted from the experimental data before determining the excitonic saturation intensity. This unsaturable background is much more apparent on samples measured at lower voltages supporting our contention that continuum bandedge absorption is the cause of the unsaturable loss. The zero intensity intercept of the responsivity is used with the sample transmission to determine the external quantum efficiency of the device. The sample transmission is also used to determine $\alpha_0 L$. The responsivity as a function of input intensity, the quantum efficiency and $\alpha_0 L$ are all used to create the fitting curve as shown in Fig. 3. One can see the intercept near zero and fine linearity both of which are indicators of the accuracy of the quantum efficiency and the value for $\alpha_0 L$. The slope indicates a saturation intensity of 632 kW/cm^2. Similar constructions

[2]The external quantum efficiency is wavelength dependent with a maximum value at the 1.054 μm wavelength of 0.85. The internal quantum efficiency is not wavelength dependent and is a better indicator of the photon-to-electron conversion efficiency. It ranges from 0 to 1 where the maximum internal quantum efficiency (1) is equal to the maximum external quantum efficiency (in this case 0.85).

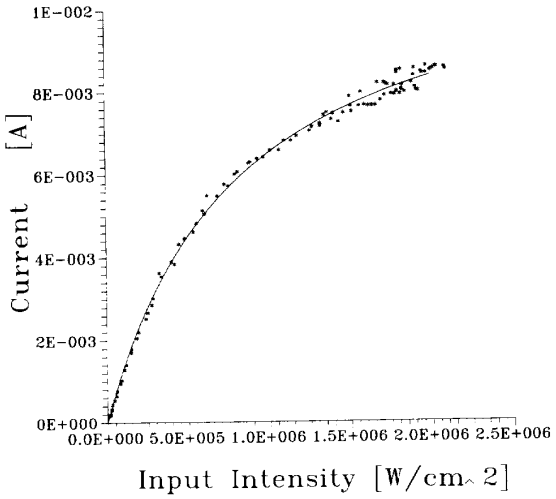

Fig. 3. Experimentally measured Photocurrent versus input laser intensity.

were performed for samples A–E with the responsivity and fitting curves shown in Figs. 5–8. The results for all the samples are tabulated in Table I.

IV. Carrier Escape Measurements

Since it is the carrier population that screens and saturates the exciton, the lifetime of the photogenerated carriers is important in determining I_s. In fact, the saturation intensity of a material is inversely proportional to its lifetime [9], [14]. In MQW modulators under a bias voltage, the lifetime is determined by the escape time of the carriers from the wells and the radiative and non-radiative recombination rate of the carriers before they escape the wells [9]. Knowledge of the escape times together with the saturation intensity can give information on the carrier population required to saturate the exciton, i.e., the saturation density.

Carrier escape from quantum wells was modelled along the following general description. Electron-hole pairs are optically generated in a series of electrically biased wells at a level consistent with the absorption coefficient of the well material and the optical intensity of the input light at that particular well (note that the input light intensity will decay as the light travels through the absorbing multiple quantum wells). Carriers escape from the wells with a characteristic exponential escape time and travel at the saturation velocity (due to the high bias field) to one of the two contact regions. The

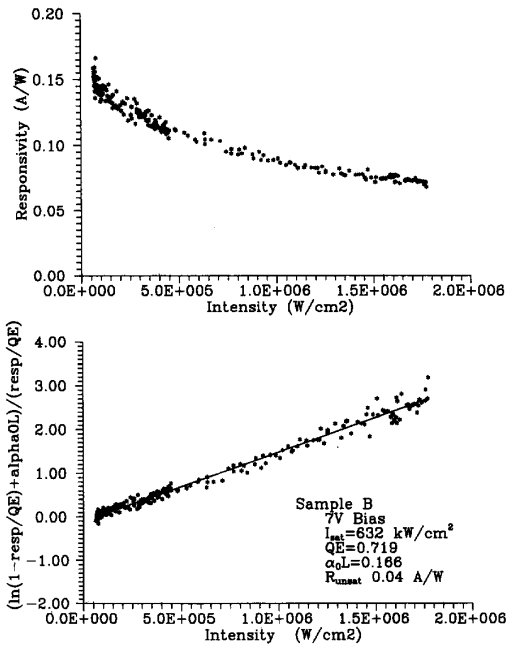

Fig. 4. Responsivity and fitting graphs for sample B.

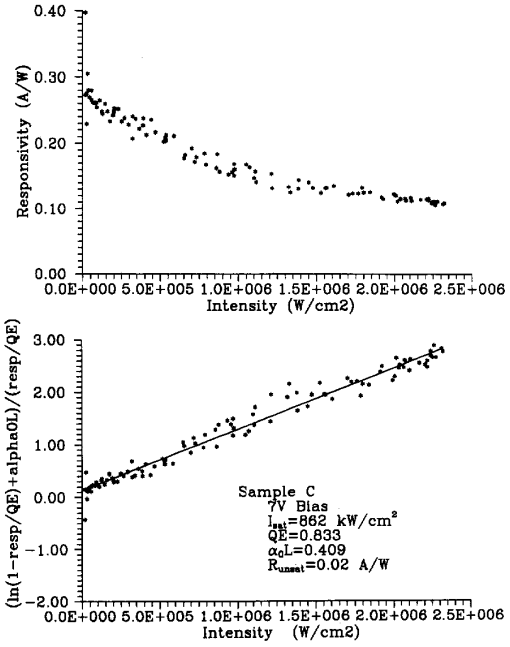

Fig. 6. Responsivity and fitting graphs for sample C.

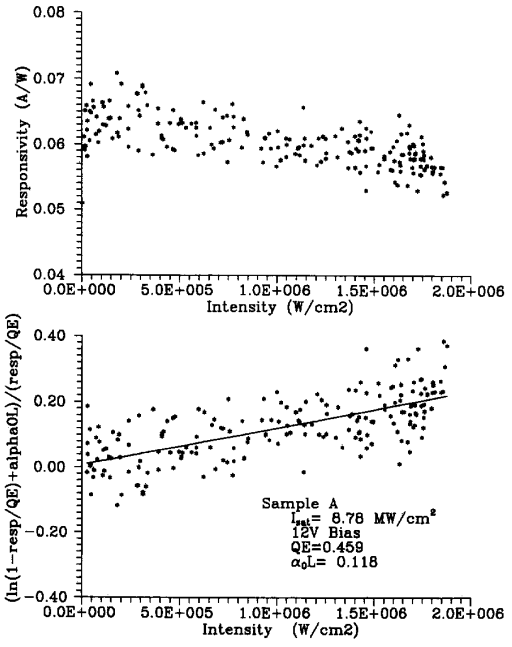

Fig. 5. Responsivity and fitting graphs for sample A.

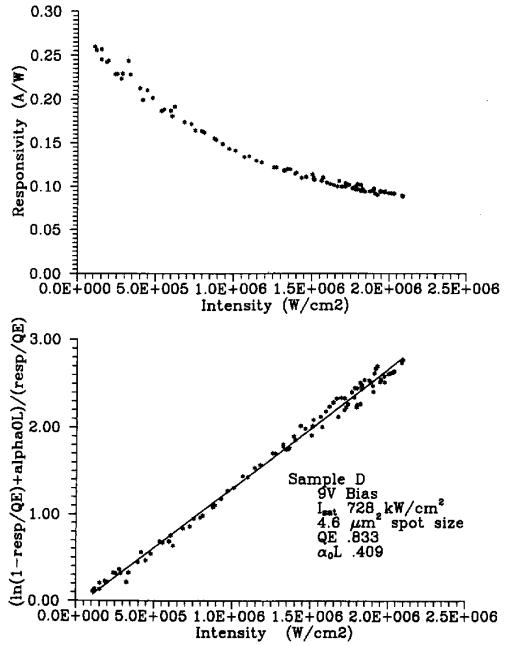

Fig. 7. Responsivity and fitting graphs for sample D.

escape times can be due to thermionic emission or tunnelling through the barrier materials. Recapture by neighboring wells is assumed to be negligible. The time that it takes the carriers to move to the contact regions is dependent upon the carrier type and distance to the appropriate contact as well as the carrier escape time from the well. Once the carriers reach the contacts they laterally spread due to diffusive conduction as described in [15]. Since the motion of the carriers through the wells and barriers is purely parallel to the applied bias field, the spatial profile of the carriers once they reach the contact region matches the input optical profile. The characteristic time to double the spatial size of the carriers after they have reached

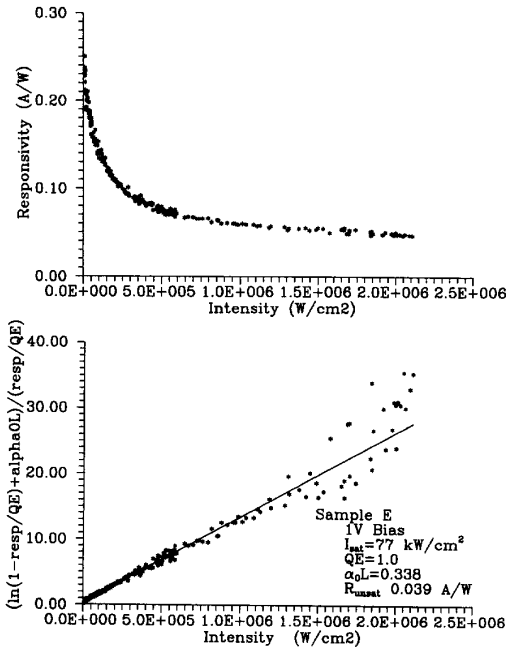

Fig. 8. Responsivity and fitting graphs for sample E. The presence of unsaturable absorption is clearest in this sample since the intensity range is much higher than the saturation intensity and the bias voltage is only 1 volt.

TABLE I

Sample	Units	A	B	C	D	E
Well Material		InGaAs	InGaAs	InGaAs	InGaAs	InAsP
Well x value		0.24	0.24	0.26	0.26	0.18
Well Thickness	Å	100	100	100	100	100
Barrier Material		GaAs	GaAs	GaAs	GaAs	InP
Barrier Thickness	Å	100	100	50	50	100
Band Gap Difference	meV	299	299	323	323	205
No. of Pairs		50	50	100	100	50
α_0	μm^{-1}	0.118	0.166	0.273	0.273	0.338
Internal QE	%	53	84	94	98	99
Bias Voltage	V	12	7	7	9	1
Unsaturated Responsivity	A/W	0.065	0.15	0.28	0.28	0.24
Unsaturable Responsivity	A/W	0.0	0.04	0.02	0.0	0.039
Saturation Intensity	kW/cm^2	8780	632	862	728	77
Hole Escape	ps	14	24	22	29	—
Electron Escape	ps	175	522	171	199	—
Effective Saturation Density N_s	$\cdot 10^{12}$cm^{-2}	17.4	5.25	2.93	2.88	—
Electron Saturation Density N_{es}	$\cdot 10^{12}$cm^{-2}	19.3	5.83	3.25	3.2	—
Hole Saturation Density N_{hs}	$\cdot 10^{12}$cm^{-2}	174	52.5	29.3	28.8	—

the contact region is called the diffusive conduction time and is given by [15]

$$\tau_c = \frac{\omega_0^2 RC}{8} \tag{10}$$

where ω_0 is the input optical $1/e$ beam radius, R is the resistance per square of the contact region, and C is the capacitance per unit area of the PIN region. Carriers which accumulate on the contacts will induce an electric field which is opposite in sign to the bias field. This induced field will alter the optical absorption of the quantum wells by the QCSE with a characteristic decay time hich is unrelated to the quantum well carrier escape times. To reduce this effect we minimized τ_c by reducing both the contact region resistance (R) and the focal spot radius (ω_0). The samples used in this study had similar contact resistances and capacitances and were all used with a 7-μm 1/ e beam radius. In this case, the diffusive conduction time for electrons was 3.1 fs and for holes was 266 fs both of which are much smaller than the escape times of $>$ 10 ps.

The photogenerated carriers affect the optical absorption in two ways. First, they screen excitons while they are inside the quantum wells. This effect tends to uniformly decrease the exciton oscillator strength and thereby the optical absorption. Second, they act to generate local electric fields that shift the exciton via the QCSE. Photogenerated carriers are polarized on either side of the well by the bias electric field prior to escape. In this case, each well is affected in the same way. Because the exciton peak was shifted to the laser wavelength by the bias electric field, any change in the electric field in the well region will also decrease the optical absorption. Thus, we see that both effects will have a time signature determined by the carrier quantum well escape rates.

A numerical simulation was performed to model the observed change in absorption for differing quantum well escape times. The carrier density in the wells is plotted using an input optical pulse of 3.5 ps. The modelling for four different escape times is shown in Fig. 9. The inserted logarithmic graph illustrates that at some time after the input pulse, the carrier rate is purely exponential with a decay equal to the escape time from the wells. Since there are two carrier types (electrons and holes) generated which both alter the applied voltage and have different escape times, the change in optical absorption will have two components. By adding the model results for two different escape times the carrier escape times (if sufficiently different) are clearly separable and can be independently determined as shown in Fig.

The carrier escape times for four of the five samples were measured at the same bias voltages used for the saturation intensity measurements. Pump-probe techniques were used to measure the change in absorption as a function of time as illustrated in Fig. 11. A passively model-locked Nd:YLF laser provided stable 3.5-ps pulses at a 250-MHz repetition rate [16]. An imaging system determined the $1/e$ beam radius on the sample surface to be 7.2 μm. A computer-controlled translation stage provided delay of the probe to map out the absorption decay. The normalized absorption change for samples A and B are shown in Fig. 12 and for sample C and D in Fig. 13. One can see that sample A has a faster decay than sample B as would be expected since it has a higher bias voltage. If the escape mechanism is by thermionic

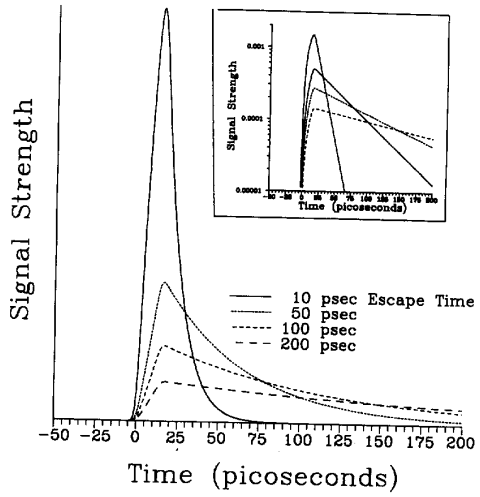

Fig. 9. Simulation of the induced absorption change due to carrier escape for carriers with escape times of 10, 50, 100, and 200 picoseconds.

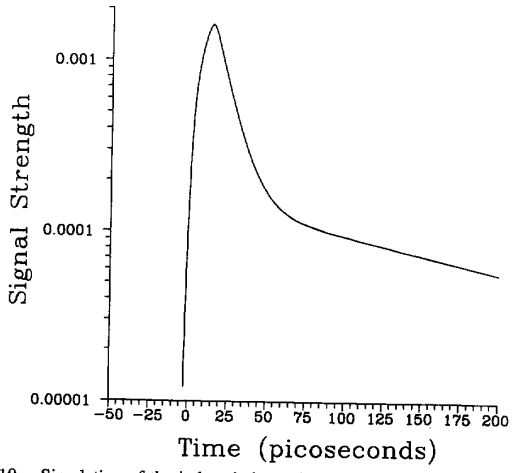

Fig. 10. Simulation of the induced absorption change due to the two carrier types having different escape times.

emission, a higher voltage results in a faster escape [9]. The two component decay is also clearly illustrated. The decay times were measured and are tabulated in Table I. The fast components of samples C and D are similar, however, the slower component of sample C is faster than sample D even though it has a lower bias voltage. This indicates that the escape mechanism is not purely due to thermionic emission which monotonically increases with bias field. To further investigate the escape mechanism the decay rates were measured on this sample for a series of voltages and the results are shown in Fig. 14. One can see a dip in the escape time near 6 V indicative of a resonant tunnelling effect [19]. This explains the higher saturation intensity for sample C at a 7-V bias than sample D at a 9-V bias since the electron escape time is faster at the 7-V bias level [9].

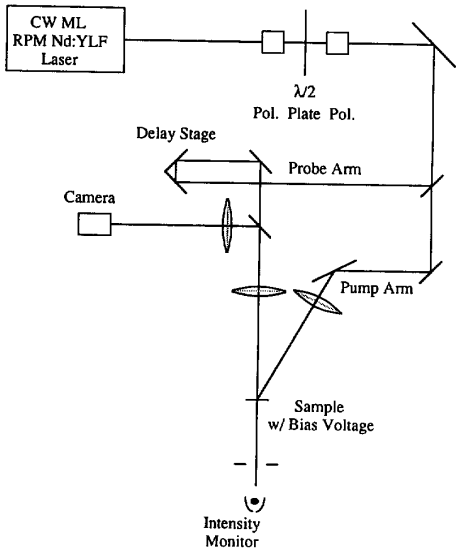

Fig. 11. Experimental setup used to make the carrier escape measurements.

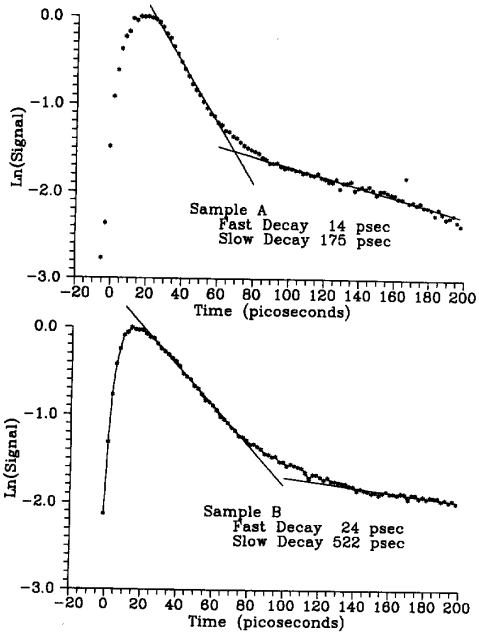

Fig. 12. Experimentally measured absorption change for samples A and B.

The escape times for sample E were not measurable. The low saturation intensity would indicate a long escape time. Long escape times would reduce the opposing field effects. In addition, if the escape time were longer than the 4 nanoseconds between pump pulses, the next pump-probe event would occur before the material had time to recover. For these reasons, and the finite length of the translation stage used to provide the probe pulse delay, consistent determinations of the escape time were impossible.

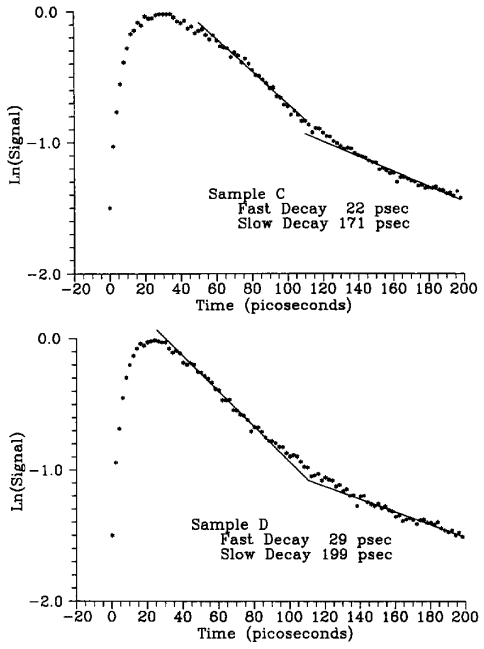

Fig. 13. Experimentally measured absorption change for sample C and D.

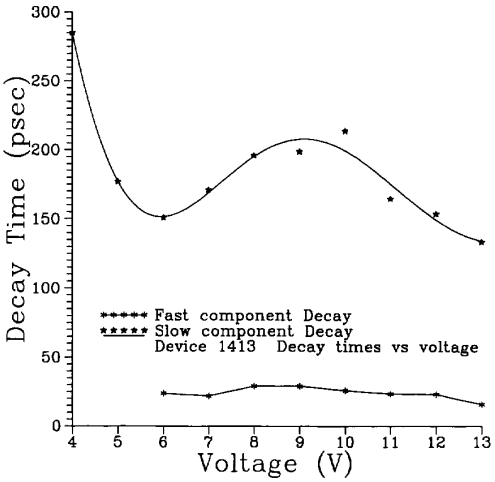

Fig. 14. Escape times for the two carrier types as a function of applied bias voltage for sample C, D.

V. Saturation Density

The saturation density for electrons and holes can be calculated using the measured saturation intensity and carrier escape times. The formalism is similar to that used in [13]. The steady-state populations for each carrier type are given by

$$N_i = \frac{I\alpha_0\tau_i[L_W + L_B]}{\hbar\omega} \qquad (i = e, h) \tag{11}$$

where L_W and L_B are the well and barrier thicknesses, respectively, I is the input optical intensity, τ_i is the carrer decay time, and $\hbar\omega$ is the input photon energy. The saturation density for a particular carrier type is proportional to the number of carriers in the region of k space defined by the exciton radius. Holes are heavier, being defined over a larger region of k space, therefore, the density can be shown to be proportional to the effective mass of the carrier as [20]:

$$N_{si} = \frac{m_i}{2\pi a_{2D}^2 \mu}\frac{kT}{E_0} = \frac{m_i}{\mu}C \qquad (i = e, h) \tag{12}$$

where a_{2D} is the $2d$ exciton radius, μ is the reduced mass, m_i is the effective mass of the carrier, and E_0 is the exciton binding energy. C is defined as a carrier independent constant. In the small signal limit the fractional change in exciton absorption due to carrier saturation can be related to two carrier types

$$-\frac{\Delta\alpha}{\alpha_0} \approx \frac{I}{I_s} = \frac{N_e}{N_{se}} + \frac{N_h}{N_{sh}}. \tag{13}$$

Inspection of (12) indicates that the saturation density of electrons will be less than that of holes since the effective mass is smaller. Since the saturation density is in the denominator of (13), it is clear that an electron will have a stronger effect upon the saturation intensity than a hole. Let us define an effective saturation density N_s by noting that when photoexciting carriers $N_e(t = 0) = N_h = N$ and

$$-\frac{\Delta\alpha}{\alpha_0} = \frac{N}{N_s}. \tag{14}$$

Equating (13) and (14) results in

$$\frac{1}{N_s} = \frac{1}{N_{se}} + \frac{1}{N_{sh}}. \tag{15}$$

Combining (12) and (15)

$$\frac{1}{N_s} = \frac{\mu}{m_e C} + \frac{\mu}{m_h C} = \frac{\mu}{C}\left(\frac{m_h + m_e}{m_e m_h}\right) = \frac{1}{C}. \tag{16}$$

Therefore, we can relate the effective saturation density to the individual carrier saturation densities

$$N_{se} = \frac{m_e}{\mu}N_s \tag{17}$$

$$N_{sh} = \frac{m_h}{\mu}N_s. \tag{18}$$

The effective saturation density can be related to the individual carrier effective masses and carrier decay times by combining (11), (12), (17), and (18)

$$N_s = \left[\frac{m_e\tau_h + m_h\tau_e}{m_e + m_h}\right]\left[\frac{\alpha_0 I_s(L_W + L_B)}{\hbar\omega}\right]. \tag{19}$$

The electron and hole decay times are not identical to the electron and hole escape times since they do not include the effects of recombination losses. If the recombination rate is separable from the escape rate then the decay time is given by

$$\frac{1}{\tau_D} = \frac{1}{\tau_{\text{esc}}} + \frac{1}{\tau_{\text{rcmb}}}. \tag{20}$$

The fast component in the experimentally measured decay is due to the hole escape from the wells. The reason for choosing the holes over the electrons is twofold. First, if one assumes

that the escape time is dominated by thermionic emission, then the ratio of hole escape time to electron escape time is

$$\frac{\tau_{Eh}}{\tau_{Ee}} = \left(\frac{m_h}{m_e}\right)^{1/2} e^{-\Delta E_g(Q_e - Q_h)/kT} \tag{21}$$

where Q_e and Q_h are the conduction and valence band offset fractions of the band gap difference which for InGaAs are 0.60 and 0.40, respectively [17].[3] In unstrained $X = 0.26$ $In_xGa_{1-x}As$ wells $m_e = 0.055m_0$ and $m_h = 0.494m_0$[18]. Strain has an effect on the in-plane hole effective mass, but the reduced mass is dominated by the electron mass. ΔE_g is the band gap difference which for our case is 299 meV. For the $x = 0.26$ $In_xGa_{1-x}As$ wells and GaAs barriers used this ratio is $\tau_{Eh}/\tau_{Ee} = 0.41$ indicating that the holes are about 2.5X faster than the electrons. The second indication that the fast component is due to holes is that the long time component exhibits resonant tunnelling behavior at a bias voltage of near 6 V as evidenced in Fig. 14. Level splitting calculations indicate that this could only be the case for electrons; resonant tunnelling effects for holes would occur at voltages of 1V or less for these samples. If one ignores recombination effects and assumes that the entire decay time is due to the escape time, then the effective saturation density is calculated using (19) and tabulated in Table I. The densities (N_s) range from $2.8 - 17 \cdot 10^{12}\text{cm}^{-2}$. Low quantum efficiency devices would tend to have short recombination times since the carriers would recombine before they are swept out of the wells. Since the recombination time was not used in the calculation of the saturation density, one would expect that samples with short recombination times would cause the calculated saturation density to be higher because τ_D would be smaller than τ_{esc} as indicated by (20). Examination of Table I indicates that this is indeed the case. Samples with lower quantum efficiencies have a higher calculated saturation density.

From (16), we can make a theoretical estimate of N_s (see also [19, (3.1.9b)]) given by

$$\frac{1}{N_s} = 2\pi a_{2D}^2 \frac{E_{1S}}{kT} \tag{22}$$

where a_{2D} is the two-dimensional exciton radius and E_{1S} is the exciton binding energy. Fits to low temperature absorption data of the samples indicate a binding energy of 6 meV for the InGaAs samples and 8 meV for the InAsP samples. If one assumes that the exciton is purely two-dimensional,[4] the exciton radius is related to the binding energy by [12]

$$a_{2D} = \left(\frac{\hbar^2}{8E_{1S}\mu}\right)^{1/2} \tag{23}$$

where μ is the reduced mass. For the $x = 0.26$ $In_xGa_{1-x}As$/GaAs samples a_{2D} is 56Å which, using (22) at a temperature of 300 K, gives a saturation density of $2.1 \cdot 10^{12}\text{cm}^{-2}$. This is in remarkable agreement with the experimentally determined densities. For the $x = 0.18$ $InAs_xP_{1-x}$/InP samples a_{2D} is[5] 41 Å, which results in a theoretical saturation density of $3.0 \cdot 10^{12}$ cm^{-2}. Because of the lack of experimentally measured carrier lifetimes for sample E, we were unable to compare this number with an experimental value.

[3] We assume that the band offset at $x = 0.26$ is close to that of $x = 0.2$ as noted in [17, Table I].

[4] The excitons are not purely two-dimensional due to the 100- Å well width. The value used for a_{2D} is a lower limit.

VI. Conclusions

Saturation densities and intensities of InGaAs/GaAs and InAsP/InP multiple-quantum-well modulators are consistent with previous experimental and theoretical treatments of AlGaAs/GaAs modulators. We have measured the saturation intensity and electron and hole escape times and used the results to directly determine the saturation density. We find an experimentally determined density of $2.9 \cdot 10^{12}$ cm^{-2} determined using the theory of Schmitt–Rink *et al* . [20]. The saturation intensities were higher than those found for comparable AlGaAs/GaAs samples due to a slightly lower absorption and a presumably faster electron escape time from the wells. Comparison of the escape times measured here with those found for the AlGaAs/GaAs material system in [13] is impossible due to the different measurement methods used. Due to the similarity of the band offsets and barrier heights between the InGaAs/GaAs samples used here and the AlGaAs/GaAs samples used in [13], the difference in saturation intensity is surprising. The samples tested all had varying levels of strain and dislocations. Samples with high levels of dislocations had low quantum efficiencies due to carrier recombination at dislocation sites in the wells. This fast recombination decreases the effective carrier lifetime. Modulators with higher dislocation densities, therefore, tend to have higher saturation intensities. The higher saturation intensities together with the availability of high-power optical sources at the operating wavelength of these modulators make them attractive choices for next generation optical interconnection and processor systems.

References

[1] N. Streibl, K.-H. Brenner, A. Huang, *et al.*, "Digital optics," *Proc. IEEE*, vol. 77, p. 1954, 1989.

[2] M. E. Prise, N. C. Craft, M. M. Downs, R. W. LaMarche, L. A. D'Asaro, L. M. F. Chirovsky, and M. J. Murdocca, "Optical digital processor using arrays of symmetric self-electrooptic effect devices," *Appl. Opt.*, vol. 30, p. 2287, 1991.

[3] F. B. McCormick, A. L. Lentine, R. L. Morrison, S. L. Walker, L. M. F. Chirovsky, L. A. D'Asaro, "Parallel operation of a 32 × 16 symmetric self-electrooptic device array," *IEEE Photon. Technol. Lett.*, vol. 3, p. 232, 1991.

[4] D. A. B. Miller, "Quantum-well self-electro-optic effect devices," *Opt. Quant. Electr.*, vol. 22, p. S61, 1990.

[5] T. K. Woodward, T. Sizer, II, D. L. Sivco, and A. Y. Cho, "InGaAs/GaAs multiple quantum well optical modulators for the 1.02–1.07 μm wavelength range," *Appl. Phys. Lett.*, vol. 57, p. 548, 1990.

[6] T. K. Woodward, T. Sizer, II, and T. H. Chiu, "InAsP/InP multiple quantum well optical modulators for solid-state lasers," *Appl. Phys. Lett.*, vol. 58, p. 1366, 1991.

[7] I. J. Fritz, D. R. Myers, G. A. Vawter, T. M. Brennan, and B. E. Hammons, "Novel reflectance modulator employing an InGaAs/AlGaAs strained-layer supperlattice Fabry–Perot cavity with unstrained InGaAs/InAlAs mirrors," *Appl. Phys. Lett.*, vol. 58, p. 1608, 1991.

[8] T. Sizer, II, R. E. LaMarche, and T. K. Woodward, "Point source heating effects in multiple quantum well modulators," *Appl. Phys. Lett.* (submitted).

[5] Without a value available for the $x = 0.18$ $InAs_xP_{1-x}$ hole mass, we used the electron mass of 0.07 (from [18]) as an estimate for the reduced mass.

[9] A. M. Fox, D. A. B. Miller, G. Livescu, J. E. Cunningham, J. E. Henry, and W. Y. Jan, "Exciton saturation in electrically biased quantum wells," *J. Appl. Phys. Lett.* vol. 57, p. 2315, 1990.
[10] T. Sizer, II, T. K. Woodward, T.-H. Chiu, D. L. Sivco, and A. Y. Cho, "Optoelectronic device mapping using differential imaging techniques," *J. Appl. Phys.*, vol. 70, p. 3837.
[11] D. A. B. Miller, D. S. Chemla, T. C. Damen, *et al.*, "Band-edge electroabsorption in quantum well structures: The quantum-confined stark effect," *Phys. Rev. Lett.*, vol. 53, p. 2173, 1984.
[12] D. S. Chemla, D. A. B. Miller, P. W. Smith, A. C. Gossard, and W. Wiegmann, "Room temperature excitonic nonlinear absorption and refraction in GaAs/AlGaAs multiple quantum well structures," *IEEE J. Quant. Electr.*, vol. QE-20, p. 265, 1984.
[13] A. M. Fox, D. A. B. Miller, G> Livescu, J. E. Cunningham, and W. Y. Jan, "Quantum well carrier sweep out: Relation to electroabsorption and exciton saturation," *IEEE J. Quant. Electr.*, vol. 27, p. 2281, 1991.
[14] O. Svelto, *Principles of Lasers*. New York: Plenum, 1977, p. 57.
[15] G. Livescu, D. A. B. Miller, T. Sizer, *et al.*, "High-speed absorption recovery in quantum well diodes by diffusive electrical conduction," *Appl. Phys. Lett.*, vol. 54, p. 748, 1989.
[16] U. Keller and T.-H. Chiu, "Resonant passive modelocked Nd:YLF Laser," submitted to *J. Quantum Electr.*, submitted for publication.
[17] B. Jogai, "Valence-band offset in strained GaAs-InGaAs superlattices," *Appl. Phys. Lett.*, vol. 59, p. 1329, 1991.
[18] K.-H. Hellege, ed., *Landoli–Börnstein Numerical Data and Functional Relationships*, Vol. 17 Semiconductors, p. 219.
[19] G. Livescu, A. M. Fox, D. A. B. Miller, *et al.*, "Resonantly enhanced electron tunneling rates in quantum wells," *Phys. Rev. Lett.*, vol. 63, p. 438, 1989.
[20] S. Schmitt–Rink, D. S. Chemla, and D. A. B. Miller, "Linear and nonlinear optical properties of semiconductor quantum wells," *Adv. Phys.*, vol. 38, pp. 89–188, 1989.

T. Sizer, II, photograph and biography not available at the time of publication.

T. K. Woodward, photograph and biography not available at the time of publication.

U. Keller, photograph and biography not available at the time of publication.

K. Sauer, photograph and biography not available at the time of publication.

T.-H. Chiu, photograph and biography not available at the time of publication.

D. L. Sivco, photograph and biography not available at the time of publication.

A. Y. Cho, photograph and biography not available at the time of publication.